Title

Specific bone region localization of osteolytic versus osteoblastic lesions in a patient-derived xenograft model of bone metastatic prostate cancer

Authors

Hirata, Takeshi
Park, Seung Chol
Muldong, Michelle T
et al.

Peer reviewed

Original Article

Specific bone region localization of osteolytic versus osteoblastic lesions in a patient-derived xenograft model of bone metastatic prostate cancer

Takeshi Hirata [a], Seung Chol Park [b], Michelle T. Muldong [c,d,e],
Christina N. Wu [c,f], Tomonori Yamaguchi [g], Amy Strasner [c,d,e],
Omer Raheem [d,e], Hiromi Kumon [a], Robert L. Sah [h],
Nicholas A. Cacalano [i], Catriona H.M. Jamieson [c,f],
Christopher J. Kane [c,d,e], Koichi Masuda [g], Anna A. Kulidjian [c,g],
Christina A.M. Jamieson [c,d,e,*]

[a] *Department of Urology, Okayama University Graduate School of Medicine, Dentistry and Pharmaceutical Sciences, Okayama, Japan*
[b] *Department of Urology, Wonkwang University School of Medicine and Hospital, Iksan, South Korea*
[c] *Moores Cancer Center, University of California, San Diego, La Jolla, CA, USA*
[d] *Department of Urology, University of California, San Diego, La Jolla, CA, USA*
[e] *Department of Surgery, University of California, San Diego, La Jolla, CA, USA*
[f] *Department of Medicine, University of California, San Diego, La Jolla, CA, USA*
[g] *Department of Orthopaedic Surgery, School of Medicine, University of California, San Diego, La Jolla, CA, USA*
[h] *Department of Bioengineering, University of California, San Diego, La Jolla, CA, USA*
[i] *Department of Radiation Oncology, University of California at Los Angeles, Los Angeles, CA, USA*

Abstract *Objective:* Bone metastasis occurs in up to 90% of men with advanced prostate cancer and leads to fractures, severe pain and therapy-resistance. Bone metastases induce a spectrum of types of bone lesions which can respond differently to therapy even within individual prostate cancer patients. Thus, the special environment of the bone makes the disease more complicated and incurable. A model in which bone lesions are reproducibly induced that

* Corresponding author. Department of Urology, Department of Surgery, Moores Cancer Center, University of California, San Diego, La Jolla, CA, USA.
   E-mail address: camjamieson@ucsd.edu (C.A.M. Jamieson).

mirrors the complexity seen in patients would be invaluable for pre-clinical testing of novel treatments. The microstructural changes in the femurs of mice implanted with PCSD1, a new patient-derived xenograft from a surgical prostate cancer bone metastasis specimen, were determined.

Methods: Quantitative micro-computed tomography (micro-CT) and histological analyses were performed to evaluate the effects of direct injection of PCSD1 cells or media alone (Control) into the right femurs of $Rag2^{-/-}\gamma c^{-/-}$ male mice.

Results: Bone lesions formed only in femurs of mice injected with PCSD1 cells. Bone volume (BV) was significantly decreased at the proximal and distal ends of the femurs ($p < 0.01$) whereas BV ($p < 0.05$) and bone shaft diameter ($p < 0.01$) were significantly increased along the femur shaft.

Conclusion: PCSD1 cells reproducibly induced bone loss leading to osteolytic lesions at the ends of the femur, and, in contrast, induced aberrant bone formation leading to osteoblastic lesions along the femur shaft. Therefore, the interaction of PCSD1 cells with different bone region-specific microenvironments specified the type of bone lesion. Our approach can be used to determine if different bone regions support more therapy resistant tumor growth, thus, requiring novel treatments.

1. Introduction

Prostate cancer is the most common solid cancer in men and the second leading cause of cancer of death in men [1]. The majority of prostate cancer patients with metastatic disease will develop bone metastases. Patients with bone metastases are at risk of skeletal related events, including spinal cord compression, pathological fracture, and severe bone pain leading to surgery and/or radiation to alleviate bone pain, and prevent or repair pathologic fractures. In a recent large US study, 10% of prostate cancer patients with newly diagnosed bone metastasis already had skeletal related events (SREs) [2]. During follow-up, the cumulative incidence of SREs in these patients increased: 21.5% at 6 months, 30.4% at 12 months, 41.9% at 24 months, and 48.9% at 36 months [2]. Therefore, bone metastases contribute substantially to patients' mortality and morbidity.

Bone metastases in most men with prostate cancer are a mix of osteoblastic and osteolytic lesions [3]. The mechanisms by which prostate cancer tumor cells induce osteoblastic lesions which are characterized by new bone formation, or osteolytic lesions which are characterized by increased bone resorption leading to thinning bone are unclear. It is hypothesized that osteoblastic lesions are formed by intense osteoblastic activity, preceded by osteoclastic bone resorption in patients with prostate cancer [3]. However, it is possible that prostate tumor cells can induce metastatic bone lesions that do not involve osteoclastic activity [4]. The relative contribution of extrinsic factors from specific bone microenvironments versus factors intrinsic to the tumor cells themselves to the type of bone lesion formed is not understood. The reciprocal interaction of the tumor cells and bone microenvironment also gives rise to a pathologically altered tumor microenvironment which can drive further malignant tumor progression [5].

The type of cancer cells themselves plays a crucial role in determining the type of bone reaction both in patients and mouse models transplanted with human tumor cells.

Most of the group of cancers that often metastasize to bone such as breast, lung and kidney cancer invariably induce osteolytic lesions [2,4]. Prostate cancer, on the other hand, has a higher proportion of osteoblastic and mixed lesions compared to purely osteolytic lesions [1–5]. The complexity of the types of osseous lesions induced by bone metastatic prostate cancer in patients was comprehensively analyzed in the recent work of Vargas and co-workers in which the types of bone metastatic lesions in castration resistant prostate cancer patients were evaluated using computed tomography (CT), FDG-PET and FDHT-PET [6]. They showed a range of at least six bone lesion types classified along a spectrum from dense osteoblastic to mixed osteoblastic-osteolytic to purely osteolytic in nature even within a single patient. Patients with the highest number of bone lesions and whose lesions had the highest ^{18}F-DHT (dihydrotestosterone, DHT) uptake had the shortest overall survival [6]. Different types of osseous lesions were also investigated in the study of bone metastasis samples obtained in a rapid autopsy study from patients who had died of metastatic castrate resistant disease [7–9]. Histomorphometric analysis revealed significant heterogeneity comprising a wide range of osteolytic to osteoblastic osseous responses within individual patients [8]. The mechanisms and clinical implications of the types of prostate cancer bone metastasis lesions found even within an individual patient need to be determined. Elucidating the mechanisms underlying bone metastatic lesion formation may lead to the development of new treatments for bone metastatic prostate cancer [10].

The complexity of prostate cancer bone lesions makes them extremely challenging to study and, therefore, to develop effective treatments in patients [6,10]. Thus, there is a significant need for accurate models to investigate prostate cancer interaction with the bone microenvironment. In experimental models of cancer bone metastasis, prostate cancer cells or xenografts harvested from human rapid autopsy programs show differential osteoblastic versus osteolytic reactions in the mouse

skeleton when introduced as tumor xenografts. The LuCaP patient-derived xenograft series produced a range of intra-tibial bone reactions depending on the line [9]. The LNCaP derived cell line, C4-2-B which formed mixed osteoblastic and osteolytic lesions in mouse bone xenografts, was derived from an original lymph node metastasis of a patient [5,11]. Intra-tibial xenograft transplantation of the PC3 prostate adenocarcinoma cancer cell line derived from a patient bone marrow metastasis formed purely osteolytic lesions, while LAPC9 cells which were derived from a patient femoral bone metastasis, formed purely osteoblastic lesions [12–15]. Prostate cancer xenografts designated as MDA models, showed some of the lines are osteoblastic and others are osteolytic in which fibroblast growth factor 9 (FGF9) played a mediating role [16].

Pre-clinical studies with these models have led to significant advances in patient treatments, however, they were not always predictive of patient responses in larger clinical trials such as for the drug, cabozantinib [17,18]. This has been attributed to species-specific differences in mouse and human bone microenvironments, as well as the extensive passaging of some of these cell lines during which they have acquired documented changes from the original tumor specimen. However, prostate cancer is often highly heterogeneous within and between patients, therefore, a greater diversity and range of patient-derived xenograft (PDX) models representing more patients need to be available to test new therapies. For these reasons, we undertook the development of new PDXs of prostate cancer bone metastasis. We developed PCSD1, a new intra-femoral xenograft model of prostate cancer bone metastasis derived from a surgical bone metastasis specimen from the femur of a patient with a pathologic fracture [19]. Preliminary micro-computed tomography (micro-CT) analysis revealed that PCSD1 cells induced mixed osteoblastic and osteolytic bone lesions when transplanted into femurs of immunodeficient male mice which closely resembled the bone lesions in the patient [19]. In the current study, we quantitatively defined the microstructural changes in the murine femurs into which PCSD1 were injected using high-resolution two- (2D) and three-dimensional (3D) micro-CT.

2. Materials and methods

2.1. Patient derived xenograft tumor cells

All studies with human samples were performed with the approval of the University of California, San Diego (UCSD), School of Medicine Institutional Review Board. The patient provided written informed consent. Prostate cancer bone metastasis cells were obtained directly from the bone metastatic lesion in the proximal femur of a patient with castrate-resistant prostate cancer having a hemi-arthroplasty to treat a pathologic fracture in the right femur head. Gleason score of original tumor was 10 (5 + 5), and mixed osteoblastic and osteolytic lesions were observed in the proximal femur on CT. Tumor cells used to create the xenograft were directly derived from the original specimen or only early tumor passages and prepared according to the protocols in Raheem et al. [19].

2.2. Direct intra-femoral injection in mice

All animal protocols were approved by the UCSD animal welfare IACUC committee. Male, 6–8 week old $Rag2^{-/-}\gamma c^{-/-}$ mice were used for direct intra-femoral injection [19]. Mice were anesthetized with intra-peritoneal (i.p.) injection of a mix of 100 mg/kg ketamine and 10 mg/kg Xylazine. The right knee was held in flexed position and a 25-gauge needle (Monoject 200 25 × 5/8A) was inserted into the femoral condyle until there was no resistance. It was used as a port-hole for injection of 15 μL sample using a 0.3 mL syringe and 27-gauge needle. Sample injection was performed slowly with minimal resistance. Leg was immediately straightened after injection and held straight for approximately 1 min and antibiotic ointment applied. Mice were injected with atipa-mezole (Antisedan, Zoetis, Pasippany, New Jersey, USA) and placed on a warm DeltaPhase pad (Braintree Scientific, Braintree, MA, USA) and carefully observed until full recovery.

2.3. Micro-CT: image acquisition, processing and analysis

For quantitative micro-CT analysis 13 mice injected intra-femorally (i.f.) with PCSD1 cells plus Matrigel in which the injection site needle hole was visible through the condyle in micro-CT imaging and macroscopic tumor formation were selected for the PCSD1 group and eight mice injected i.f. with Media/Matrigel alone, with needle hole in the condyle were selected for the Control group. Mice were sacrificed 8–10 weeks after injection. Inferior limbs were carefully harvested from all mice, and fixed in 10% neutral buffered formalin. Femurs were scanned on a SkyScan 1076 micro-CT scanner (Bruker, Kontich, Belgium), and regions of interest (ROIs) were determined using established guidelines [20]. Parameters analyzed by micro-CT included total cross-sectional tissue area (Tt.Ar), cortical bone area (Ct.Ar), cortical area fraction (Ct.Ar/Tt.Ar), cortical thickness (Ct.Th), tissue mineral density (TMD), tissue volume, bone surface (BS), bone volume (BV), trabecular thickness (Tb.Th), trabecular spacing (Tb.Sp), trabecular number (Tb.N), structure model index (SMI), and bone mineral density (BMD), bone mineral content (BMC), and tissue mineral content (TMC) [20]. Femurs were imaged and acquired using the micro-CT SkyScan 1076 (Bruker, Kontich, Belgium) at a source power of 59 kV/167 μA and spatial resolution of 9.06 μm/pixel with 0.5 mm-thick aluminum filter. The rotation was set at 0.7° per step for 180°. Samples were set into 50 mL centrifuge tube and packed with saline wettened gauze to prevent hydration and movement during scanning.

2.4. Image processing

The reconstructions were performed with NRecon software package (SkyScan) to obtain transaxial grayscale images [21]. Each ROI was delineated so as to include both sides of the whole femur. 2D transaxial, coronal, and sagittal images were obtained with Data Viewer software (SkyScan) based on the ROI data [21]. The longitudinal axis along the femur (on the coronal and sagittal images) was set parallel to the bone shaft, and transaxial images

along this axis were used to create 3D images or to analyze bone quantity [21]. The longitudinal axis was determined by two independent researchers (TH and TY). Micro-CT visualization of the needle hole through the growth plate at the condyle was used as confirmation of successful intra-femoral injection on the 2D and 3D images.

2.5. Micro-CT 3D imaging

To create 3D micro-CT-based femur models, the 2D trans-axial images were imported in the 3D reconstruction of each femur using the 3D reconstruction software package Mimics 14.12 (Materialise NV, Plymouth, MI, USA). Femur length was measured on the 3D image from the top of greater trochanter to the top of the medial condyle. The maximum diameter of the bone shaft was also measured on the 3D image. Measurement of femur length and maximum femur diameter was performed by two independent researchers (TH and TY).

2.6. 2D radiographic image analysis for bone quantification

The parameters for bone quantity were analyzed in the whole femur bone, the condyle area, the middle of the bone shaft (cortical bone area), the proximal bone area and trabecular bone. The whole femur bone length was measured from the top of the medial condyle to the bifurcation of the femur neck at the top of greater trochanter. Different bone regions expressed as percentage of this total length to take into account the variation in femur lengths between mice. The condyle region was measured from the top of the condyle to the growth plate. Cortical bone area was measured from the midpoint of the total femur length. The cortical bone area for each sample was proportionally adjusted, or normalized, to the relative longitudinal value as a percentage of the length of the longest femur as detailed in Supplemental fig. 1. The proximal bone area of each femur head was measured from the bifurcation of the femur neck which was defined as the end of proximal area and normalized as percentage of the longest femur as detailed in Supplemental fig. 1. The trabecular bone area of the femur was measured from the growth plate, an important landmark for trabecular area, and extending proximally 10.92% of total femur length (Supplemental fig. 1).

2.7. Bone quantity analysis

All parameters for bone quantity analysis were calculated automatically with CT-Analyzer software. Bone threshold values were determined by the Otsu method [22] in Skyscan CT-Analyzer Software (Bruker, Kartuizersweg 3B, 2550 Kontich, Belgium). In condyle and proximal bone analysis, total bone volume was defined as the outer surface outline as described in Bouxsein guidelines [20] and in Supplemental fig. 2A. In cortical bone analysis, total bone volume was defined as external cortical surface and outside edge of endocortical surface (Supplemental fig. 2B). BV is defined as the volume of the region segmented as bone while total volume (TV) is the volume of the entire region of interest including soft tissue and the space inside the bone. The TV measurement software/algorithm approximates the irregular surface and small porosity as smooth surface. TV of condyle, proximal bone, and cortical bone was determined with an automated "Shrink wrap" method (21, Supplemental fig. 2). TV of trabecular bone was defined as irregular and anatomic region of interest drawn manually a few voxels away from the endocortical surface [21] as shown in Supplemental fig. 2. Bone volume per total volume (BV/TV), bone surface density (BS/TV), open porosity (Po(op)), total porosity (Po(tot)), mean Tb.Th, mean Tb.N, mean Tb.Sp, trabecular pattern factor (Tb.Pf), SMI were computed using a marching-cubes algorithm and calculated on 3D image [20,21]. Cross-sectional BV and cross-sectional thickness (Cs.Th) were calculated on 2D images.

2.8. Statistical analysis

The results of bone quantity parameters were expressed as the mean $\pm$ SD. The student's t-test, Welch's test, and Mann–Whitney's U test were used to determine significant differences between two independent groups. The student's t-test was used under the condition that both groups had normal distributions and equal variances. Welch's test was used under the condition that both groups had normal distributions but non-equal variances. Mann–Whitney's test was used when each group had non-normal distribution. Normal distributions were confirmed with Shapiro–Wilk W test, and equal variances were confirmed with F test. One-way analysis of variance (ANOVA) was used for comparison among three individual groups. All tests were considered significant when $p < 0.05$. All statistical analysis was performed with JMP 10 (SAS Institute Inc., Cary, NC, USA).

2.9. Histology

After micro-CT scanning, the left and right legs which were already fixed in 10% formalin prior to micro-CT scanning were decalcified with 10% EDTA then embedded in optimum cutting temperature compound (OCT, Tissue-Plus, Fisher Scientific, USA) and frozen in isopentane/dry ice bath for cryosections or paraffin embedded as described in Raheem et al. [19]. Sagittal plane 5 μm sections were stained with hematoxylin and eosin (H&E). To examine the histological structure as well as the distribution and content of proteoglycan, multichromatic FAST staining was also used which comprised Alcian blue, safranin O, tartrazine, and fast green dyes was performed as previously described [23]. Images were captured using the Aperio ScanScope (Leica Biosystems, Buffalo Grove, IL, USA) and Keyence digital microscopes (Itasca, IL, USA).

3. Results

3.1. Micro-CT analysis of PCSD1-injected mouse femurs revealed osteolytic and osteoblastic bone lesion formation

Quantitative microstructural analysis was performed on the femurs from mice directly injected with either PCSD1 cells or
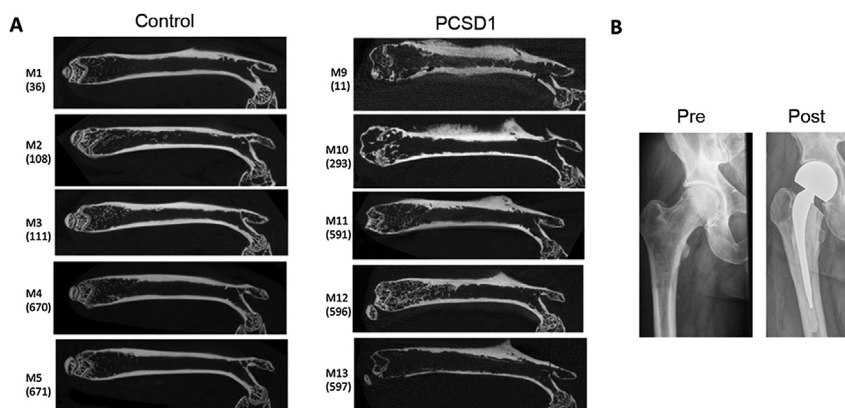
Figure 1   2D micro-CT images of Control-injected (Matrigel alone) and PCSD1-injected $Rag2^{-/-}\gamma_c^{-/-}$ mouse femurs and X-ray of the PCSD1 xenograft donor patient's femur pre- and post-hemi-arthroplasty. (A) Representative coronal 2D micro-CT of images from five mice each of the Control group and the PCSD1 group. Mouse numbers M1—M5 for the Control group in which the right femur was directly injected with Matrigel/media alone are shown (total number of mice in Control group, $n = 8$). Mouse numbers M9—M13 are shown for the PCSD1 group in which the right femur was injected with PCSD1 cells in Matrigel (total number of mice in PCSD1 group, $n = 13$). (B) X-ray of the PCSD1 xenograft donor patient's femur pre- and post-hemi-arthroplasty. The numbers on the brackets refer to the mouse identification numbers in our records and can be deleted from the figure.

with Media Control. For this study, successful intra-femoral injection was confirmed by the presence of the injection hole in the micro-CT scan of the femur condyle. Two dimensional images of the femurs were compared between the Control ($n = 8$) and PCSD1 ($n = 13$) groups (Fig. 1). Significant hypertrophic changes and high bone density regions were seen along the cortical bone in the PCSD1-injected right femurs particularly on the lateral side compared to the Matrigel/media-injected right femurs of the Control group (Fig. 1). In contrast, most of the PCSD1-injected femurs showed low bone density at the distal condyle, trabecular region and in the proximal femur head. A minor sub-group of PCSD1 samples showed hypertrophic changes in the trabecular bone. Fractures were also detected in some of the PCSD1 groups of femurs as seen in Fig. 2 near the femur head. Bone reaction or bone lesions were not seen in the un-injected, contra-lateral (Fig. 2A and Supplemental Fig. 3A, B, C) femurs of either the Control or PCSD1 group.

The donor patient's X-rays pre- and post-right hip hemiarthroplasty are shown in Fig. 1B. An abnormal, permeative pattern of bone destruction of the proximal femur metadiaphysis was identified consistent with metastatic disease (Fig. 1B). The lesion was approximately 10 cm in length and occupied the entire width of the femur. There was a subtle, undisplaced crack through the medial femoral cortex just below the lesser trochanter consistent with an

undisplaced pathologic fracture. Subtle periosteal reaction is present just inferior to the lower trochanter at the fracture site. Abnormal sclerotic foci are seen. Pathology showed metastatic prostatic adenocarcinoma. Thus, the intra-femoral xenograft, PCSD1, of the patient's bone metastatic tumor cells replicated the osteolytic lesion at the proximal femur including periosteal reaction and fracture. In addition, the sclerotic features were consistent with osteoblastic features in the PDX.

Structural changes were examined in 3D micro-CT images of the injected femurs as shown in Fig. 2 and Supplemental fig. 3. Osteolytic lesions were seen especially in the distal condyle area and in the proximal area of the femur head which had porous bone full of small cavities. In contrast, the cortical bone along the length of the femur was broader and showed irregular, jagged extensions especially on the lateral side (Fig. 2 and Supplemental fig. 3) [24].

3.2. PCSD1 tumor cells were located within osteolytic and osteoblastic bone lesions

In order to determine the location of PCSD1 tumor cells relative to the bone microstructure features observed in micro-CT analysis, H&E histochemical staining was performed on sagittal sections of the legs from the same
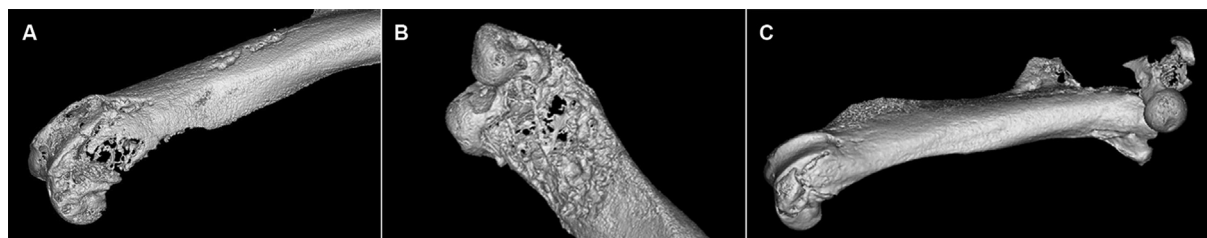
Figure 2   3D micro-CT images of PCSD1-injected condyle and whole femur showing osteolytic bone reaction in (A) the distal femur (condyle), (B) the distal femur underside (condyle, underside) (C) osteoblastic reaction along lateral side of femur shaft osteolytic reaction and fracture at proximal femur head.

mice. Comparing the knee joints of the injected femurs showed that the femur condyle of the Control (Matrigel plus media-only, Fig. 3A, left panel), contained bone marrow cells (green arrows), while the endosteal space of the femur condyle from the PCSD1-injected femur was filled PCSD1 tumor cells (black arrow, Fig. 3A, right panel). The tibia of both the Control and PCSD-1 injected mice contained only bone marrow cells (green arrows). At higher magnification the PCSD1 tumor cells (yellow arrow, Fig. 3B, top right panel) were observed growing within the femur directly adjacent to the bone (dark blue arrow). PCSD1 tumor cells seen in Fig. 3B grew within the femur endosteum and within the mixed osteolytic and osteoblastic lesions with periosteal bone reaction (medium blue arrow) and also invaded the adjacent skeletal muscle (light blue arrow). Comparison of H&E stained cortical periosteal regions sagittal sections of PCSD1-injected femurs showed tumor cells adjacent to regions of periosteal reaction along femur shaft and osteoblastic bone formation (Supplemental fig. 4).

Masson's trichrome staining was performed on femur sections to visualize collagen and bone (blue), keratin and muscle fibers (red), cytoplasm (light red or pink), and cell nuclei (dark brown to black). As shown in Fig. 3C the multi-nucleated osteoclast cells (red arrow) were present in bone resorption bays in the distal femur in an osteolytic lesion. In Fig. 3D, a hypertrophic region of newly forming bone can be seen in the proximal femur neck region. Ossifying endochondral cells in the zone of cartilage calcification were surrounded by osteoblasts (green arrow). Thus, within the bone lesions there are PCSD1 tumor cells, osteoclasts in lytic regions and osteoblasts in regions of rapid bone formation and periosteal reaction.

3.3. Quantitative 2D micro-CT bone measures showed osteolytic lesions were localized to distal and proximal ends while osteoblastic lesions were localized along the cortical bone

In order to corroborate the visual observations, tumor-induced changes in bone structure were quantified including: total femur length, BV at the distal and proximal ends and along the shaft of the femur in micro-CT analysis.
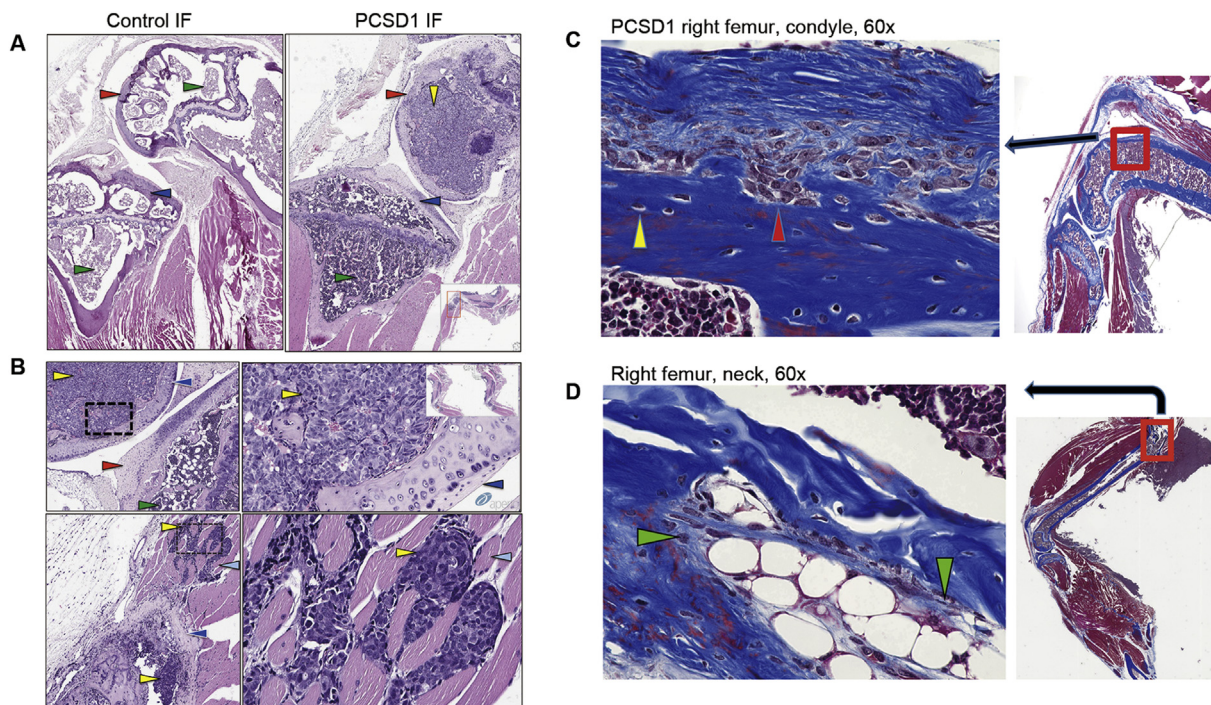
Figure 3 Histology of sagittal sections of PCSD1- compared to Control-injected mice. (A) Images of H&E stained sections through the knee joints of Control (left panel) and PCSD1 (right panel) injected mice at 200× magnification. Inset lower right shows H&E images of sagittal sections of whole right leg. (B) Top panels: PCSD1 cells within femur condyle adjacent to bone. Bottom panels: Image of PCSD1 tumor cells (yellow arrows) within femur endosteum (lower yellow arrow) and muscle-invading PCSD1 prostate cancer cells (upper yellow arrow), dark blue arrow shows femur bone, light blue arrow shows skeletal muscle fibers. Right, lower panel shows 200× magnified image of muscle-invading PCSD1 tumor cells (yellow arrow). Green arrow shows bone marrow cells, red arrow shows femur condyle bone, dark blue shows bone, black arrow shows PCSD1 prostate cancer cells. Inset shows H&E images of serial sagittal sections of whole right leg. (C) Masson's trichrome staining of femur sections showed osteoclasts present in lytic regions and osteoblasts in regions of rapid bone formation and periosteal reaction. Sections of PCSD1-injected femur sections stained with Masson's trichrome which stained keratin and muscle fibers (red), collagen and bone (blue), cytoplasm (light red or pink), and cell nuclei (dark brown to black). Multi-nucleated osteoclast cells (red arrow) present in bone resorption bays in the distal femur in an osteolytic lesion. (D) Hypertrophic region of newly forming bone can be seen in the proximal femur neck region with mixed osteolytic and osteoblastic bone reaction. Large, white cells are maturing cartilage cells in zone of cartilage calcification surrounded by osteoblasts (green arrows).

The femur length of the injected, right leg was compared to the uninjected, left leg in both the Control and PCSD1 groups. Interestingly, the right, injected femurs were shorter than the left, uninjected femurs in both the Control group and the PCSD1 group (Supplemental fig. 5). The intra-femoral injections were performed in six to eight week old mice which are still in the late stages of development. This analysis revealed the negative influence on bone growth of the injection through the growth plate in the condyle of the femur. Therefore, importantly, the comparisons of quantification of bone changes were performed only between the injected, right femurs comparing the effects of injecting the Control (media plus Matrigel alone) to the injection of PCSD1 cells.

The cross-sectional BV was determined along the longitudinal axis of the whole bone using the 2D micro-CT images (Fig. 4). BV and TV were measured at four specific locations along the length of the bone: condyle, trabecular bone, cortex, and proximal bone as shown in Fig. 4A. Their locations along the length of the femur are shown in Fig. 4B. The ratio of the mean cross-sectional BV/TV ratio along the length of the femur is plotted in Fig. 4C. The BV/TV ratio was lower in the spongy, porous bone at the condyle and proximal ends of the femur and increased along the cortical, dense bone in the shaft of the femurs in Control

femurs shown as the blue line in Fig. 4C. The changes in the BV/TV ratios in PCSD1 femurs (red line) were the opposite of those in the Control group. PCSD1 group had significantly less BV expressed as lower BV/TV ratios at the ends of the bone in the condyle and proximal femur than the Control group. Conversely, the cortical bone area along the shaft of the femur had significantly increased BV and BV/TV ratio in the PCSD1 compared to the Control group. In trabecular bone area (trabecular bone and cortical bone outside the trabecular bone), the BV of PCSD1 group and Control group were almost same. Therefore, the transition in BV along the longitudinal axis showed decreased BV at the ends and increased BV along the femur shaft of the PCSD1 group compared to the Control group.
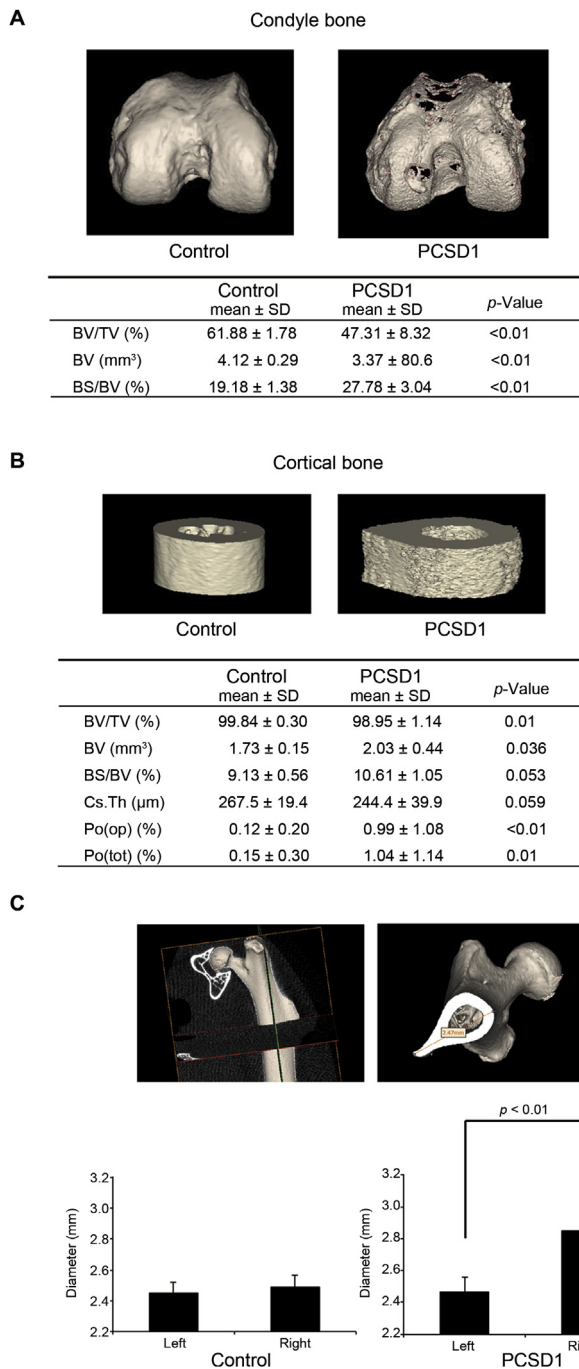
3.4. Distal condyle and proximal femur ends had significantly lower BV in PCSD1-injected femurs in 3D micro-CT analysis

Analysis of BV in 3D micro-CT images was performed on the condyles of PCSD1 and Control femurs. The condyle of the femur forms part of the knee joint and consists of spongy bone. BV/TV of the PCSD1 group was significantly less than the Control group (47.31 ± 8.32)% vs. (61.88 ± 1.78)%,
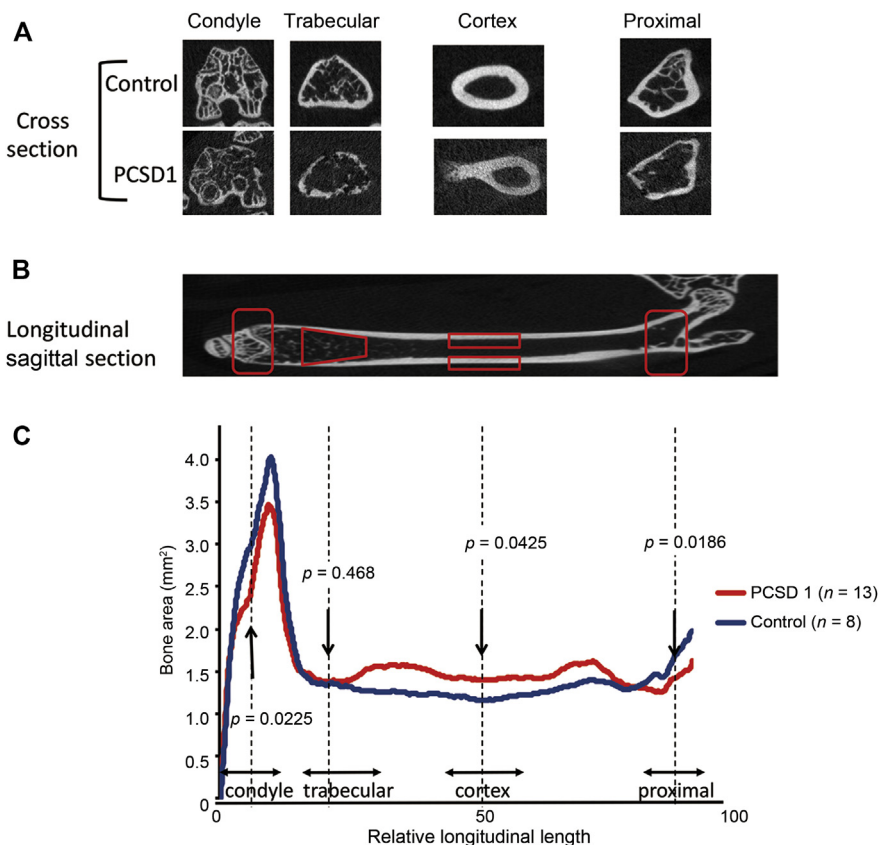
Figure 4 Comparison of 2D micro-CT images between Control and PCSD1 groups showed reciprocal transitional changes in bone volume along length of the femur. Quantitation of bone volume in serial cross-sections along the longitudinal axis of the whole bone was calculated on 2D micro-CT images. (A) Axial cross-section micro-CT images through condyle, trabecular region, cortex and proximal femur of Control and PCSD1-injected femurs. Injection site needle holes can be seen in condyle cross-sections. (B) Corresponding quantified regions along the longitudinal axis of sagittal 2D micro-CT sections of the right femur. (C) Bone volume (mm^3) in each region was plotted against relative position along femur length (expressed as relative length segmental image slices).

A

Condyle bone

	Control mean ± SD	PCSD1 mean ± SD	p-Value
BV/TV (%)	61.88 ± 1.78	47.31 ± 8.32	<0.01
BV (mm³)	4.12 ± 0.29	3.37 ± 80.6	<0.01
BS/BV (%)	19.18 ± 1.38	27.78 ± 3.04	<0.01

B

Cortical bone

	Control mean ± SD	PCSD1 mean ± SD	p-Value
BV/TV (%)	99.84 ± 0.30	98.95 ± 1.14	0.01
BV (mm³)	1.73 ± 0.15	2.03 ± 0.44	0.036
BS/BV (%)	9.13 ± 0.56	10.61 ± 1.05	0.053
Cs.Th (μm)	267.5 ± 19.4	244.4 ± 39.9	0.059
Po(op) (%)	0.12 ± 0.20	0.99 ± 1.08	<0.01
Po(tot) (%)	0.15 ± 0.30	1.04 ± 1.14	0.01

C

Figure 5 3D Micro-CT analysis revealed decreased bone volume (BV) at the end of femur in the condyle but increased BV, porosity and bone shaft diameter in cortical bone in PCSD1-injected femurs compared to Control-injected femurs. (A) Analysis of BV in 3D micro-CT images was performed on the condyles of PCSD1 and Control femurs. The condyle of the femur forms part of the knee joint and consists of spongy bone. BV and BV/TV of the PCSD1 group was significantly less than the Control group. Consistent with this, the ratio of bone space to bone volume (BS/BV) of the PCSD1 group was significantly more than the Control group. (B) Cortical bone along femur shaft had higher BV and porosity in PCSD1-injected femurs than Control-injected femurs. PCSD1 group had significantly more BV than Control group in cortical bone area, whereas BV/TV in PCSD1 group was

$p < 0.01$). Consistent with this, the BS/BV ratio of the PCSD1 group was significantly more than the Control group (Fig. 5A).

The proximal end of the femur forms part of the hip joint and also consists of spongy bone. Like the condyle, the BV/TV of the proximal femur of the PCSD1 group was significantly less than the Control group (40.97 ± 9.04)% vs. (55.45 ± 2.37)%, $p < 0.01$). Likewise, the BS/BV ratio of the PCSD1 group was significantly more than the Control group (Supplemental fig. 6).

3.5. Cortical bone had significantly increased BV, porosity and maximum diameter of the femur bone shaft in PCSD1-injected femurs

The PCSD1 group had significantly higher BV in the cortical bone area than the Control group (Fig. 5B, 2.03 ± 0.44 vs. 1.73 ± 0.15 mm³, $p = 0.036$) which was consistent with qualitative observations of 2D and 3D images (Figs. 1 and 2). Unexpectedly, the ratio of BV/TV in PCSD1 group was slightly lower than the Control groups (98.95 ± 1.14)% vs. (99.84 ± 0.30)%, $p = 0.01$). While the maximum diameter of the bone shaft in PCSD1 group was larger than Control group (Fig. 5B), the mean Cs. Th which takes into account the density as well as overall volume of the bone showed no significant difference between two groups. This apparent discrepancy was revealed to be due to increased porosity of the cortical bone of the PCSD1 group. The ratio of BS/BV, Po(op) and Po(tot) which indicate irregularity of the bone group was significantly increased in PCSD1 group than Control group (Fig. 5B).

Many samples in the PCSD1 group showed greater hypertrophic, osteoblastic changes on the lateral side of the bone shaft as seen in 2D and 3D micro-CT images (Figs. 1 and 2, Supplemental Fig. 3). The maximum diameter of the bone shaft at the third trochanter was measured to quantify these changes. The maximum diameter of the right bone shaft at the third trochanter in PCSD1 group was significantly larger than of the left, uninjected femur, whereas there was no significant difference in Control group between the right and left third trochanters (Fig. 5C).

3.6. Trabecular bone was a transitional zone

Overall the PCSD1 group showed no significant differences among the bone quantity parameters in the trabecular bone

lower than Control group. The maximum diameter of the bone shaft in PCSD1 group was longer than Control group, however, the mean thickness of the bone shaft (Cs. Th) showed no significant difference between two groups. BS/BV, open porosity (Po(op)) and total porosity (Po(tot)) which indicate irregularity of the bone group showed greater ratio in PCSD1 group than Control group. (C) PCSD1 tumor growth increased the maximum diameter of the femur bone shaft. The maximum diameter of the bone shaft was measured to quantify these changes. The maximum diameter of the right bone shaft in PCSD1 group showed significantly larger diameter than left femur, whereas there was no significant difference in Control group.

except for BV, the ratio of BS/BV and trabecular thickness (Tb.Th) (Supplemental Table 1). BV and BS/BV in PCSD1 group were higher than Control group and the PCSD1 group had thinner trabeculae (Tb.th) than the Control group. While there was no significant difference in the BV/TV ratio between PCSD1 group and Control group, there was wide range of deviation within the PCSD1 group.

To further characterize the variability of the trabecular bone in the PCSD1 group, the PCSD1 group was divided into two sub-groups: the high BV/TV group ($n = 7$) and low BV/TV group ($n = 6$) (Supplemental Fig. 7). All parameters were re-evaluated and compared among these three sub-groups. In this analysis, these three groups showed significant difference in almost all parameters except for trabecular separation (Tb.Sp). Thus, trabecular bone demonstrated a more complex combination of changes in BV, trabecular structure and porosity indicating that it seems to be a transitional zone between spongy and cortical bone such that the net effect of PCSD1 tumor growth on the trabecular bone can tilt in either direction and perhaps may be affected by factors such as the exact location of injection within the endosteal space, tumor cell deposition site, initial tumor growth site and tumor size.

4. Discussion

Different types of bone lesions typically occur within an individual prostate cancer patient, however, the mechanism that determines why a specific type of bone lesion forms is not understood [6]. In this study we performed quantitative 2D and 3D micro-CT analysis of bone lesions in our new PDX model of bone metastatic prostate cancer, PCSD1. PCSD1 formed osteolytic, osteoblastic and mixed bone lesions when directly injected into the endosteal space in the femur of $Rag2^{-/-}\gamma_c^{-/-}$ male mice that were similar to those seen in the donor patient. We noticed that the osteolytic bone lesions appeared to be restricted to the distal and proximal ends of the femur while the osteoblastic lesions consistently formed along the femur shaft in the cortical bone. Quantitative analyses of bone microstructures corroborated these qualitative observations and established that the BV was significantly lower at the ends of the PCSD1 tumor cell-injected femurs and aberrantly high along the lateral side of the femur shaft compared to controls. Intriguingly, bone reactions in the trabecular bone region which connects the ends of the bone to the cortical bone were mixed but could be sub-divided into primarily osteo-lytic or osteoblastic in nature, and thus, may reflect a transition zone between different bone microenvironments. This is the first report of reproducible, regional localization of bone microenvironment-specific differences in the types of prostate cancer-induced bone lesions in any PDX model.

The reproducible regional specificity of the types of bone lesions that formed in our PCSD1 model leads us to hypothesize that the PCSD1 cells interact with bone-niche and bone region-specific cell types that regulate osteolytic versus osteoblastic bone responses. Osteolytic bone response may be due to preferential activation of osteo-clasts in the spongy bone at the ends of the femur and/or inhibition of osteoblasts and their bone forming functions in response to PCSD1 cells. Conversely, the osteoblastic

response in the long bone region of the femur shaft may be due to increased osteoblast activation. However, a strong periosteal reaction indicative of rapid tumor growth in concert with increased bone porosity was also seen in these regions. This may indicate that an osteolytic reaction pre-cedes and/or coincides with osteoblastic bone growth as has been previously described in other xenograft models and in studies of bone turnover markers in patients with bone metastatic prostate cancer [3,11]. The time dependence of the bone lesion formation and consequent BV differences in the proximal, distal and cortical regions of the bone will now be investigated at earlier time points in the PCSD1 model to further investigate the possible coupling of osteoblastic response following initial osteoclastogenesis.

Interestingly, the intermediate region of trabecular bone showed mixed lesions that could be sub-classified as predominantly osteolytic or osteoblastic. This fits with the model that the relationship between location and the type of bone lesion formed may be a gradient rather than a distinct border and that the trabecular bone is a transi-tional zone.

Regional localization of different cells within the bone marrow has been shown to support different functional capacities of human hematopoietic stem cells in bone marrow biopsies and xenograft models [25]. Guezguez and coworkers [25] showed that hematopoietic stem cells (HSCs: CD45RA$^-$CD34$^+$CD38$^-$) from human bone marrow biopsies that had full self-renewal and multi-lineage po-tential were preferentially isolated from the trabecular bone area in the ends of the femur compared to the long bone area or shaft. The full HSC function was attributed to their location in the trabecular bone area where they physically associated with osteoblasts and mesenchymal stem cells in rather than being solely a cell autonomous property. Therefore, this work showed that anatomical regions within the bone and bone marrow dictated the function and heterogeneity of HSC cells. The specific interaction of HSCs with specialized cells within the different bone niches regulated HSC function via a non-cell autonomous mechanism [25].

In cancer, bone niche-dependent localization has been shown to regulate response to therapy. Goff and coworkers [26] demonstrated that quiescent, therapy-resistant leu-kemia stem cells were located at the endosteum. In this study, chronic myelogenous leukemia stem cells (CML-SCs) were purified from bone marrow of CML patients in blast crisis (BC-LSCs) who were resistant to the standard-of-care tyrosine kinase inhibitor (TKI), dasatinib. The cells were transplanted into $Rag2^{-/-}\gamma_c^{-/-}$ mice where they showed resistance to same therapy but only if they were located in the bone marrow. The resistant BC-LSCs were preferen-tially located in the endosteum. Therefore, spatial location of normal hematopoietic stem cells and cancer stem cells in the bone marrow have been shown to regulate their sur-vival and functional regenerative capacities as well as their sensitivity to targeted therapeutic agents [26].

Prostate cancer bone metastases often become resistant to standard therapies including androgen deprivation, ra-diation and chemotherapy. Despite the overall survival and bone benefits shown in the AFFIRM and PREVAIL trials the majority of these enzalutamide-treated advanced prostate

cancer patients still progressed and died of bone metastatic prostate cancer [18]. New bone metastasis therapies are targeted against osteolytic lesions such as denosumab, anti-RANKL, and TGFbetaRII inhibitor [27—29]. However, the osseous lesions at prostate cancer bone metastatic sites in prostate cancer are predominantly osteoblastic types of differ from other cancers such as breast cancer bone metastases which are typically purely osteolytic. Thus, these therapies are effective in reducing the osteolytic component in prostate bone metastatic lesions but there is no current treatment for osteoblastic lesions [18]. A model in which bone lesions are reproducibly induced in the different bone regions would be invaluable for measuring the effects of different therapies on the type of bone lesions that arise from the interaction of tumor cell and different bone microenvironments. Our PCSD1 model with reproducible bone lesion formation and bone-region specific types of bone lesions allows for a systematic, quantitative investigation of the mechanisms and the effects of current therapies such as the anti-androgen, enzalutamide alone or in combination with novel therapies. We showed that PCSD1 tumor cells were resistant to anti-androgen therapy specifically in the bone-niche [30]. Therefore, the PCSD1 intra-femoral xenograft model can be used to determine quantitatively the effects of current treatments such as enzalutamide and/or docetaxel on survival of prostate cancer cells in the spongy versus cortical bone-niches and determine which of these niches may perhaps preferentially support prostate cancer stem cells or castrate-resistant prostate cancer cells [30].

Conflicts of interest

The authors declare no conflict of interest.

Acknowledgments

Appendix A. Supplementary data

Supplementary data related to this article can be found at http://dx.doi.org/10.1016/j.ajur.2016.09.001.

References

[1] Siegel R, Ma J, Zou Z, Jemal A. Cancer statistics. CA Cancer J Clin 2014;64:9—29.

[2] Oster G, Lamerato L, Glass AG, Richert-Boe KE, Lopez A, Chung K, et al. Natural history of skeletal-related events in patients with breast, lung, or prostate cancer and metastases to bone: a 15-year study in two large US health systems. Support Care Cancer 2013;21:3279—86.

[3] Garnero P, Buchs N, Zekri J, Rizzoli R, Coleman RE, Delmas PD. Markers of bone turnover for the management of patients with bone metastases from prostate cancer. Br J Cancer 2000;82: 858—64.

[4] Brown JE, Neville-Webbe H, Coleman RE. The role of bisphosphonates in breast and prostate cancers. Endocr Relat Cancer 2004;11:207—24.

[5] Shiao SL, Chu GC, Chung LW. Regulation of prostate cancer progression by the tumor microenvironment. Cancer Lett 2016;380:340—8.

[6] Vargas HA, Wassberg C, Fox JJ, Wibmer A, Goldman DA, Kuk D, et al. Bone metastases in castration-resistant prostate cancer: associations between morphologic CT patterns, glycolytic activity, and androgen receptor expression on PET and overall survival. Radiology 2014;271:220—9.

[7] Roudier MP, Morrissey C, True LD, Higano CS, Vessella RL, Ott SM. Histopathological assessment of prostate cancer bone osteoblastic metastases. J Urol 2008;180:1154—60.

[8] Morrissey C, Roudier MP, Dowell A, True LD, Ketchanji M, Welty C, et al. Effects of androgen deprivation therapy and bisphosphonate treatment on bone in patients with metastatic castration-resistant prostate cancer: results from the University of Washington Rapid Autopsy Series. J Bone Min Res 2013;28:333—40.

[9] Larson SR, Zhang X, Dumpit R, Coleman I, Lakely B, Roudier M, et al. Characterization of osteoblastic and osteolytic proteins in prostate cancer bone metastases. Prostate 2013;73:932—40.

[10] Nandana S, Chung LW. Prostate cancer progression and metastasis: potential regulatory pathways for therapeutic targeting. Am J Clin Exp Urol 2014;2:92—101.

[11] Thalmann GN, Rhee H, Sikes RA, Pathak S, Multani A, Zhau HE, et al. Human prostate fibroblasts induce growth and confer castration resistance and metastatic potential in LNCaP Cells. Eur Urol 2010;58:162—71.

[12] Kaighn ME, Lechner JF, Narayan KS, Jones LW. Prostatic carcinoma: tissue culture cell lines. Natl Cancer Inst Monogr 1978;49:17—21.

[13] Kaighn ME, Narayan KS, Ohnukl Y, Lechner JF, Jones LW. Establishment and characterization of a human prostatic carcinoma cell line (PC-3). Invest Urol 1979;17:16—23.

[14] Lee Y, Schwarz E, Davies M, Jo M, Gates J, Wu J, et al. Differences in the cytokine profiles associated with prostate cancer cell induced osteoblastic and osteolytic lesions in bone. J Orthop Res 2003;21:62—72.

[15] Hsu WK, Virk MS, Feeley BT, Stout DB, Chatziioannou AF, Lieberman JR. Characterization of osteolytic, osteoblastic, and mixed lesions in a prostate cancer mouse model using ^{18}F-FDG and ^{18}F-fluoride PET/CT. J Nucl Med 2008;49: 414—21.

[16] Li ZG, Mathew P, Yang J, Starbuck MW, Zurita AJ, Liu J, et al. Androgen receptor-negative human prostate cancer cells induce osteogenesis in mice through FGF9-mediated mechanisms. J Clin Invest 2008;118:2697—710.

[17] Nguyen HM, Ruppender N, Zhang X, Brown LG, Gross TS, Morrissey C, et al. Cabozantinib inhibits growth of androgen-sensitive and castration-resistant prostate cancer and affects bone remodeling. PLoS One 2013;8:e78881.

[18] Vignani F, Bertaglia V, Buttigliero C, Tucci M, Scagliotti GV, Di Maio M. Skeletal metastases and impact of anticancer and bone-targeted agents in patients with castration-resistant prostate cancer. Cancer Treat Rev 2016;44:61—73.

[19] Raheem O, Kulidjian AA, Wu C, Jeong YB, Yamaguchi T, Smith KM, et al. A novel patient-derived intra-femoral xenograft model of bone metastatic prostate cancer that recapitulates mixed osteolytic and osteoblastic lesions. J Transl Med 2011;9:185.

[20] Bouxsein ML, Boyd SK, Christiansen BA, Guldberg RE, Jepsen KJ, Müller R. Guidelines for assessment of bone

microstructure in rodents using micro-computed tomography. J Bone Min Res 2010;25:1468—86.

[21] http://www.skyscan.be/next/ctan_usermanual.pdf#search= %20CTan+manual%20.

[22] Otsu N. A threshold selection method from gray-level histograms. IEEE Trans Sys, Man, Cyber 1979;9:62—6.

[23] Dempster DW, Compston JE, Drezner MK, Glorieux FH, Kanis JA, Malluche H, et al. Standardized nomenclature, symbols, and units for bone histomorphometry: a 2012 update of the report of the ASBMR Histomorphometry Nomenclature Committee. J Bone Min Res 2013;28:2—17.

[24] Cook MJ. The Anatomy of the Laboratory Mouse. London: Academic Press 1965. Adapted for the web by Mouse Genome Informatics: The Jackson Laboratory Bar Harbor, Maine April 2005, Revised February 2008.

[25] Guezguez B, Campbell CJ, Boyd AL, Karanu F, Casado FL, Di Cresce C, et al. Regional localization within the bone marrow influences the functional capacity of human HSCs. Cell Stem Cell 2013;13:175—89.

[26] Goff DJ, Court Recart A, Sadarangani A, Chun HJ, Barrett CL, Krajewska M, et al. A Pan-BCL2 inhibitor renders bone-marrow-resident human leukemia stem cells sensitive to tyrosine kinase inhibition. Cell Stem Cell 2013;12:316—28.

[27] Juárez P, Guise TA. TGF-β in cancer and bone: implications for treatment of bone metastases. Bone 2011;48:23—9.

[28] Casimiro S, Mohammad KS, Pires R, Tato-Costa J, Alho I, Teixeira R, et al. RANKL/RANK/MMP-1 molecular triad contributes to the metastatic phenotype of breast and prostate cancer cells in vitro. PLoS One 2013;8:e63153.

[29] Xu W, Zhang Z, Yang Y, Hu Z, Wang CH, Morgan M, et al. Ad5/48 hexon oncolytic virus expressing sTGFβRIIFc produces reduced hepatic and systemic toxicities and inhibits prostate cancer bone metastases. Mol Ther 2014;22: 1504—17.

[30] Godebu E, Muldong M, Strasner A, Wu CN, Park SC, Woo JR, et al. PCSD1, a new patient-derived model of bone metastatic prostate cancer, is castrate-resistant in the bone-niche. J Transl Med 2014;12:275.